Multi-Band Transmission Over E-, S-, C- and L-Band With a Hybrid Raman Amplifier

Pratim Hazarika [ORCID], Henrique Buglia [ORCID], Mindaugas Jarmolovičius [ORCID], Eric Sillekens [ORCID], Mingming Tan [ORCID], Aleksandr Donodin [ORCID], Ian Phillips [ORCID], *Member, IEEE*, Paul Harper [ORCID], Robert I. Killey [ORCID], Polina Bayvel [ORCID], *Fellow, IEEE*, and Wladek Forysiak [ORCID]

(Top-Scored Paper)

Abstract—Capacity enhancement by utilising the unused spectral bands of the low-loss optical window of standard single-mode fibre (SSMF) is a cost-effective solution for meeting the future demand of data traffic. The development of optical amplifiers that can operate in different spectral bands is expected to play an integral part in the establishment of multi-band networks. In this work, we perform experimental, analytical and numerical modelling of a multi-band transmission system using a hybrid distributed-discrete Raman amplifier enabling signal amplification from 1410–1605 nm. The developed amplifier was tested over 50 km of SSMF using 200 Gbit/s channels, where successful transmission was achieved, well above the HD-FEC threshold of 8.5 dB. Further study on the multi-band transmission performance was carried out using a semi-analytical closed-form approximation and split-step Fourier method-based simulations for various related test cases. The analytical and numerical models are also compared with experimental results, showing reasonable agreement in terms of system performance estimation.

Index Terms—Multi-band transmission, Raman amplifier, optical amplifier, ultra-wideband transmission, Gaussian noise model.

I. INTRODUCTION

O PTICAL fibre communication has witnessed numerous milestones over the past two decades with the implementation of compact and highly efficient optical amplifiers and state-of-the-art digital coherent technology [1]. Today, digital coherent optics has increased the capacity per twin-channel up to 1.6 Tb/s with digital signal processing (DSP) enabled by an application-specific integrated circuit (ASIC) on 7 nm complementary metal-oxide semiconductor (CMOS) technology in the form of pluggable modules [2]. Despite this incredible progress with integrated transceivers, the telecommunications sector is seeing a continual increase in global data traffic. Hence, the scientific community is exploring various technologies to sustain this global data demand. Data scaling with advanced modulation formats and constellation shaping is a cost-effective solution with minimal infrastructural upgrades. However, this approach is not a long-term solution as the channel capacity is ultimately bounded by the nonlinear Shannon limit [3].

Capacity enhancement through the spatial domain, known as space division multiplexing (SDM), is a novel technique that can enable petabyte/s data transmission over a single fibre [4]. Numerous experimental demonstrations have shown achievable data rates up to 10.66 Pbit/s using 38-core fibre [5]. SDM has also been demonstrated for unrepeated systems with an achieved throughput of 372 Tb/s over 213 km [6]. In terms of long-haul systems, a record transmission distance of 8027 km with 4-core fibre has been reported in [7]. However, this technology requires a full-scale upgrade of network infrastructure, entailing significant capital expenditure.

Multi-band transmission (MBT), on the other hand, is an interesting data scaling approach that requires relatively low investment in new infrastructure [8]. MBT utilises the unused spectral bands of the telecommunications window of standard single-mode fibre (SSMF), increasing its overall transmission capacity to hundreds of terabit/s. However, the inclusion of the entire optical window from O- to L-band requires the design and development of new commercial-grade equipment [9], [10], such as multi-band transceivers [11], re-configurable add-drop multiplexers (ROADMs) [12], [13] and optical amplifiers [14].

Focusing on optical amplifiers, the existing Erbium-doped fibre amplifier (EDFA) can support the C- and L-band with bandwidths recently extended up to 6 THz in the so-called "super" C-band and "super" L-band [15], [16]. Operating WDM systems beyond these bands requires the design and development of optical amplifiers that can enable amplification over the O-, E-, S- and U-bands [14]. Amplifiers based on rare-earth materials

Pratim Hazarika, Mingming Tan, Aleksandr Donodin, Ian Phillips, Paul Harper, and Wladek Forysiak are with the Aston institute of Photonic Technologies, Aston University, B4 7ET Birmingham, U.K. (e-mail: p.hazarika@aston.ac.uk; m.tan1@aston.ac.uk; a.donodin@aston.ac.uk; i.phillips@aston.ac.uk; p.harper@aston.ac.uk; w.forysiak@aston.ac.uk).

Henrique Buglia, Mindaugas Jarmolovičius, Eric Sillekens, Robert I. Killey, and Polina Bayvel are with the Optical Networks Group, Department of Electronic and Electrical Engineering, University College London, WC1E 7JE London, U.K. (e-mail: henrique.buglia.20@ucl.ac.uk; min.jarmolovicius.17@aston.ac.uk; e.sillekens@ucl.ac.uk; r.killey@ucl.ac.uk; p.bayvel@ucl.ac.uk).

such as bismuth, neodymium, and praseodymium are potential candidates, with numerous recent demonstrations over each of these bands [17], [18], [19]. Semiconductor optical amplifiers (SOAs) are also an interesting candidate that canprovide seamless wide-band amplification [20]. Experimental demonstrations with a combination of SOA and distributed Raman amplifier have shown amplification over the C- and L-band, with a net throughput of 99.35 Tb/s over a 257 km unrepeated system [21].

The discrete Raman amplifier (DRA), the distributed Raman amplifier (DiRA), and the hybrid combination of discrete and distributed Raman amplifier (DDRA), each based on Raman scattering in optical fibre, form a separate category of optical amplifier with high potential for ultra-wideband amplification in MBT systems [22]. The physical mechanism of the Raman amplification enables arbitrary gain anywhere in the optical fibre transmission window, where the bandwidth and gain can be tuned by the appropriate selection of wavelengths and powers of the pump laser sources [23]. Experiments with Raman amplification in distributed and discrete modes have been demonstrated over the past few years for MBT systems [24]. A transmission distance of 3040 km over C- and L-band was successfully shown by Krzczanowicz et al., with a dual-stage DRA [25]. Similarly, in the S-, C- and L-band, amplification bandwidths of 150 and 135 nm have also been achieved using a dual-stage and dual-band DRA [26], [27]. DRAs have also been demonstrated over the E-, S-, C- and L-band, where an amplification bandwidth of 210 nm was achieved and 200 Gbit/s per channel transmission was performed over signals in the range of 1410–1605 nm potentially enabling a transmission bandwidth of 21.8 THz [28], [29].

Together with experimental designs and demonstrations using Raman amplifiers, real-time nonlinear modelling of MBT is an essential tool to introduce intelligence, achieve the best resource allocation and maximise system throughput in optical networks [30], [31]. For Raman amplified links, one way of achieving that goal is using analytical expressions of the Gaussian noise (GN) model in the presence of Raman amplification [32], [33]. Such real-time prediction enables an efficient and fast design of the Raman pumps, achieving the desired amplification gain dynamically in the network [34], [35].

In this paper, we present detailed experimental results, combined with analytical and numerical modelling of MBT enabled by the hybrid DDRA presented in [36]. The proposed DDRA was experimentally characterized using modulated signals from 1410–1605 nm, corresponding to 195 nm overall bandwidth. The DDRA was then tested as an in-line amplifier over a transmission span comprising 50 km of SSMF. Our experimental results with 30 GBaud PM-16-QAM signals showed good quality transmission, well above the hard-decision forward error correction (HD-FEC) threshold of 8.5 dB. Detailed modelling of the hybrid DDRA and the resulting MBT performance was performed using semi-analytical closed-form expressions of the GN model, together with split-step Fourier method (SSFM) simulations. The modelling results show a maximum Q^2-factor deviation of 1.8 dB over the entire bandwidth when compared

to experimental results. The analytical model was further used to study the performance of a fully loaded E-band system with additional pump configurations, enabling the analysis of a future experimental setup upgrade, not presently possible experimentally due to equipment limitations.

The paper is divided into six sections. Section II describes the characterisation of the developed DDRA to estimate the amplifier gain, noise figure (NF) and output OSNR. Section III is divided into two parts, Section III-A describes the 200 Gbit/s transmission setup with hybrid DDRA and Section III-B discusses the transmission results. Section IV provides the detailed derivation of the analytical model used to estimate the transmission system performance with the hybrid DDRA. Similarly, Section V is divided into three parts, Section V-A details the parameters used for modelling the full-scale E-, S-, C- and L-band transmission using the analytical GN model and SSFM simulations. Subsection V-B describes the validation of the analytical model, while Section V-C describes the WDM system performance predictions obtained using this model, and their comparison with the experimentally obtained data, together with the analysis of additional relevant scenarios.

II. DESIGN AND CHARACTERIZATION OF THE HYBRID DDRA

The architecture of the hybrid DDRA amplifier is illustrated in Fig. 1(a), and was designed to amplify signals covering the E-, S-, C- and L-band from 1410–1605 nm. In the S- C- and L-band, a WDM grid comprises 143x100 GHz amplified spontaneous emission (ASE) dummy channels from 1470–1605 nm. The channels from 1470–1520 nm (S-band) were generated using an in-house supercontinuum source and a commercial S-band wavelength-selective-switch (WSS) for equalization, followed by a commercial thulium-doped fibre amplifier (TDFA). Similarly, the channelised ASE channels from 1530–1605 nm (C- and L-band) were generated using two independent C- and L-band EDFAs followed by two WSSs. In the absence of the availability of a commercial WSS in the E-band, we used independent diode lasers at 1411, 1431 and 1450 nm, coupled together with a 30 Gbaud PM-16-QAM signal at 1457 nm, to characterize the amplifier in the targeted bandwidth. The relative power of the WDM spectra before and after the SSMF and after the DDRA stage is shown in Fig. 1(b)–(d). These relative powers correspond to the power level obtained using a 99/1 tap whose 1% arm was connected to the optical spectrum analyser at a resolution bandwidth of 0.1 nm for capturing the traces shown in Fig. 1(b)–(d). A higher noise floor can be seen at the input spectrum of Fig. 1(b) in the 1470–1520 nm region, primarily due to the higher ASE noise generated by the supercontinuum source and the TDFA. In contrast, the lower ASE noise floor in the 1530–1605 nm region in Fig. 1(b) is due to the lower NF of the C- and L-band EDFAs.

Raman amplification was performed in either distributed or discrete fashion for the two different bands identified in Fig. 1(a). The shorter wavelengths from 1410–1457 nm were amplified using distributed amplification over the 50 km SSMF using three pump diodes at wavelengths and powers of 1325 nm (439 mW),
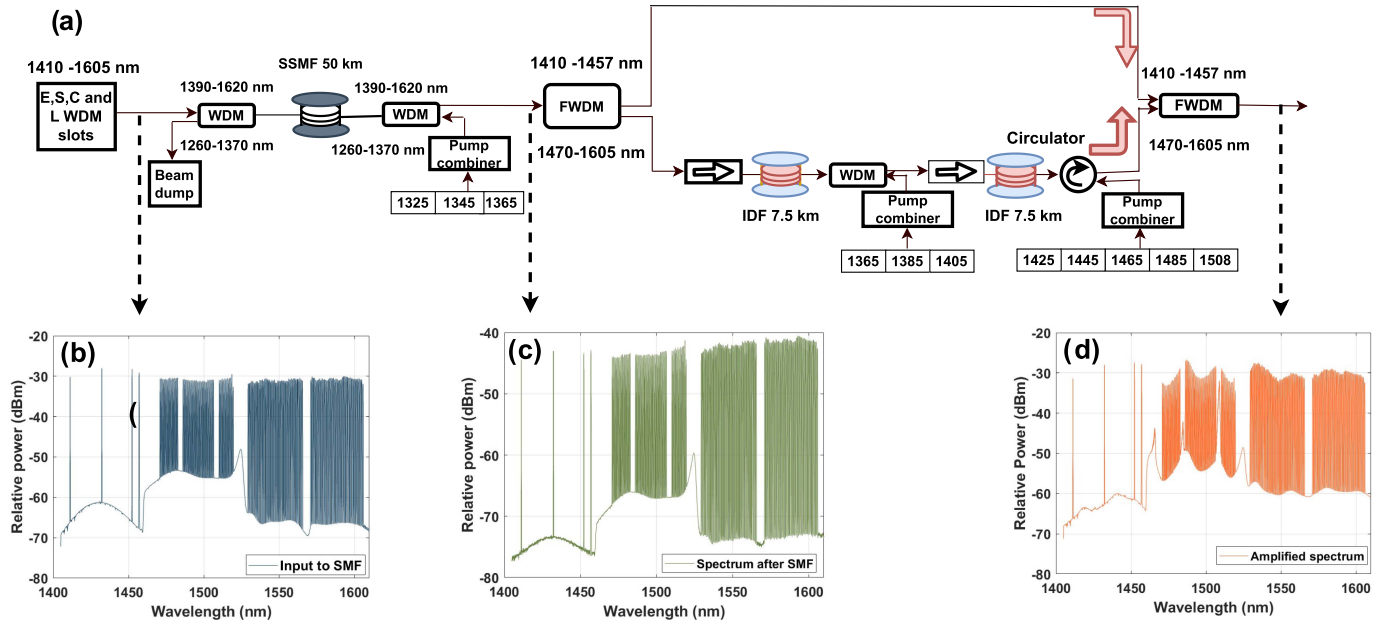
Fig. 1. Ultra-wideband hybrid distributed-discrete Raman amplifier: (a) amplifier schematic; (b) input spectrum to SSMF; (c) output spectrum after SSMF without amplification; (d) amplified output spectrum.
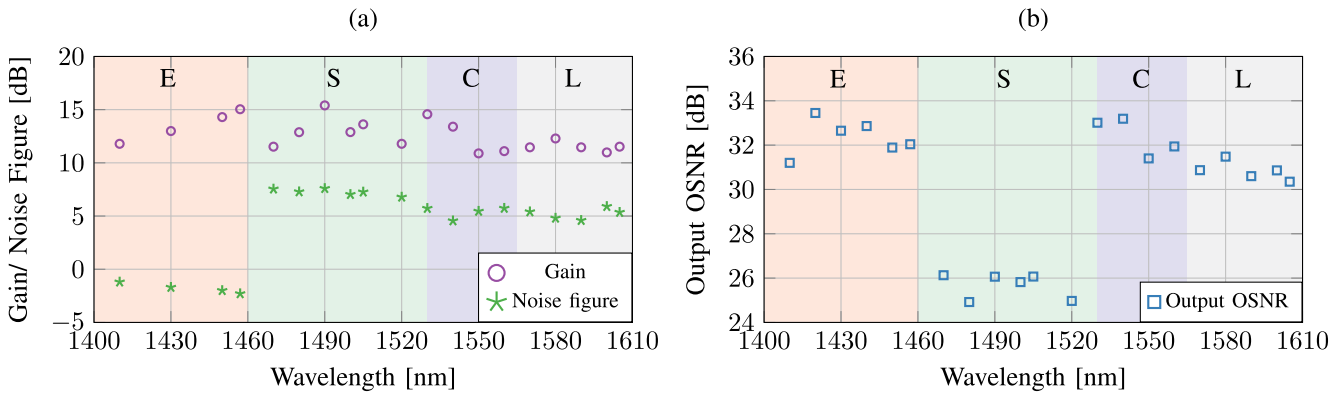

Fig. 2. Ultra-wideband hybrid distributed-discrete Raman amplifier experimentally measured: (a) gain and noise figure / effective noise figure; (b) output OSNR.

1345 nm (153 mW), and 1365 nm (318 mW). These signals were then separated using a filtered WDM (FWDM) with a passband from 1260–1464 nm and a reflection band from 1470–1620 nm to direct the E-band signals along the top arm of the DDRA, and prevent them from entering the discrete amplifier. Similarly, after exiting the reflection band of the FWDM, the S-, C- and L-band signals from 1470–1620 nm were directed along the bottom arm of the DDRA and amplified in two independent stages using a cascaded dual-stage DRA [26]. Two inverse dispersion fibres (IDF) of 7.5 km each, were used as an amplifying medium [37], pumped using 8 laser diodes of 1365 nm (495 mW), 1385 nm (212 mW), 1405 nm (170 mW), 1425 nm (294 mW), 1445 nm (312 mW), 1465 nm (198 mW), 1485 nm (110 mW) and 1508 nm (170 mW), respectively. The design of the cascaded DRA was such that the first stage preferentially amplified the signals from 1470–1520 nm, while the second stage preferentially amplified the signals from 1570–1605 nm [38], [39]. The amplifier pump

powers were adjusted to compensate for the combined loss of the SSMF and the 2 x WDM couplers, with an average loss of 14.2 dB across the band. Guard bands of $\pm$ 2 nm were inserted in the vicinity of the 1485 nm and 1508 nm pumps to prevent overlapping between the pumps and signals [40].

As noted above, the characterised hybrid DDRA has an overall average gain of just over 14 dB across the entire bandwidth shown in Fig. 2(a). However, higher gain is required locally for the E- and S- band signals due to the higher fibre loss in these bands, and inter-channel Raman scattering (ISRS) power transfer from the shorter to longer wavelengths. The overall DDRA has a maximum NF of $\sim$7.5 dB in the shorter part of the S-band, due to the DRA, and a minimum effective NF below 0 dB, in the E-band, due to the DiRA. The average NF in the S-band was observed to be $\sim$7 dB. In the C- and L-band, an average NF of $\sim$5.5 dB was measured with a maximum of 5.9 dB at 1600 nm. The measured amplifier output optical
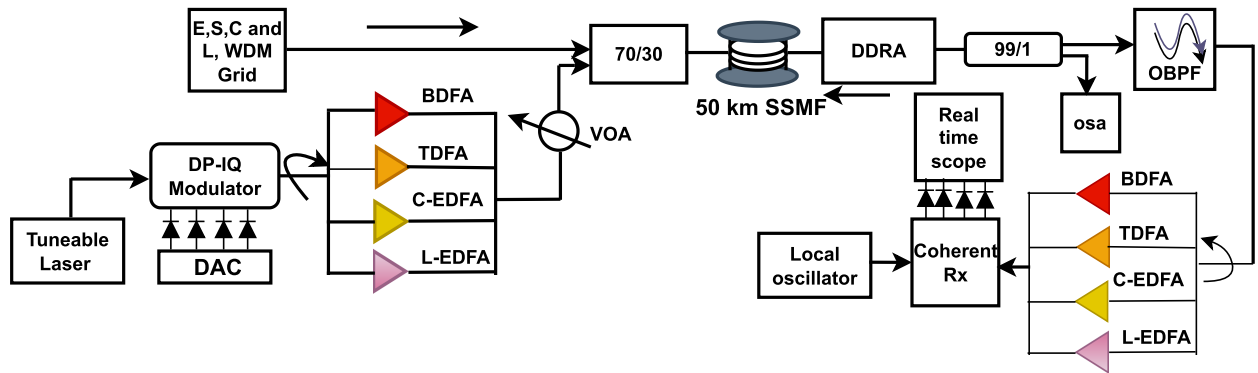
Fig. 3.   Experimental setup for 30 Gbaud PM-16-QAM transmission with 146 WDM channels over 50 km SSMF.

signal-to-noise ratio (OSNR) is shown in Fig. 2(b). The OSNR was measured after the amplifier stage using 30 GBaud PM-16-QAM signals at 10 nm intervals with the 3-point method of OSNR calculation in a noise bandwidth of 0.1 nm [41], which was calibrated over different wavelengths, as explained in [42]. The output OSNR was observed to be more than 30 dB for the E-, C- and L- band signals, and less than 27 dB for S-band signals. The reduced OSNR in the S-band region is partly due to the high NF of the dual-stage DRA, and additional ASE noise due to the supercontinuum source and TDFA used for channel equalisation.

III. COHERENT TRANSMISSION WITH THE HYBRID DDRA

In this section, we describe the performance of the developed DDRA when used as the receive stage of a 50 km transmission link with 30 GBaud PM-16-QAM test signals coupled with 146 x 100 GHz channelised ASE to represent the co-propagating WDM spectrum.

A. Experimental Setup

The developed amplifier was tested using a 200 Gbit/s per channel coherent transmission system in the experimental setup shown in Fig. 3. The coherent transmission was performed using the WDM grid shown in section II coupled together with 30 GBaud PM-16-QAM test signals, generated using a 120 GSa/s digital to analog converter (DAC) and a Lithium-Niobate (LiNbO$_3$) DP-IQ modulator. The modulated signal was amplified with the corresponding booster amplifier comprising of an in-house BDFA in the E- band with a gain of 27.3 dB and maximum output power of 20.3 dB operable within a wavelength range from 1400–1490 nm [43]. The S-, C- and L- band booster amplifier included a TDFA (1470–1520 nm) with maximum output power of 19 dBm, or a C- or L-band EDFA (1530–1620 nm) with maximum output power of 23 dBm according to the wavelength of test channel. The amplifiers were operated to enable a signal gain of ∼22 dB. A variable optical attenuator (VOA), placed after the booster amplifiers, equalised the power of the modulated test signal to the same level as the WDM grid, to which it was then added using a 70/30 coupler, for onward propagation through 50 km of SSMF. The total input power to the SSMF was ∼17.6 dBm with a power per channel of

∼−4 dBm. In the E-band region, the PM-16-QAM signal was swept across six wavelengths at 1410, 1420, 1430, 1440, 1450 and 1457 nm, while in the S-, C- and L-band it was swept at an interval of 10 nm from 1470–1600 nm and to 1605 nm, totaling 21 measurement wavelengths, as illustrated in Fig. 4(a)–(c). The propagated spectrum was then amplified using the hybrid DDRA described in section II, and divided using a 99/1 tap, whose 1% arm measured the output OSNR, while the remaining 99% power was passed through an optical bandpass filter (OBPF) to filter out the modulated signal. The filtered signal was then passed through a corresponding pre-amplifier (BDFA, TDFA, C- or L-band EDFA) ahead of the coherent receiver operating at a fixed output power of ∼8 dBm. The coherent receiver included an 90° optical hybrid and four high-speed photodetectors for balanced detection. An 80 GSa/s oscilloscope with 36 GHz bandwidth was used to capture the corresponding traces which were processed using an offline digital signal processing (DSP) chain for data recovery, and the corresponding Q^2-factor was calculated for square constellations using the measured bit error rate (BER) [44].

B. Experimental Results and Discussion

The performance of the developed DDRA over the 50 km of SSMF is illustrated in Fig. 4(a)–(c). The experimentally measured B2B Q^2-factor shows an average value of ∼17 dB in the C- and L-band region which then rolls off by ∼2 dB in the S- and E- bands. The reduced B2B Q^2-factor in the S-band is due to the higher ASE noise of the supercontinuum source and the increased NF of the TDFA used for generating the WDM grid, which can also be seen in Fig. 1(b). In the E-band, where the ASE generation and amplification are less noisy than in the S-band, the reduced B2B Q^2-factor is primarily due to the use of non-optimal commercial C-band components (transceivers) at these wavelengths, an effect which becomes more apparent with decreasing wavelength [42], [45]. The Q^2-factor after 50 km transmission and amplification by the DDRA follows a similar trend as the B2B measurements, with minimum values of 12.8 and 12.6 dB at 1410 and 1470 nm. The Q^2-factor penalty (Q^2-factor difference between B2B and 50 km transmission) shown in Fig. 4(b) can be correlated to the OSNR and NF of the DDRA. In the C- and L-band, a fairly consistent ∼1 dB penalty was
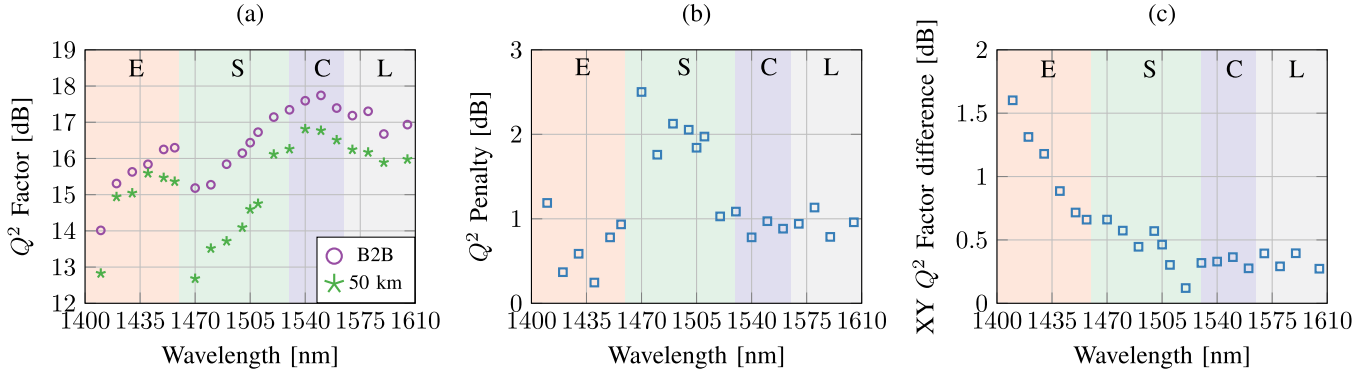
Fig. 4. 30 GBaud PM-16-QAM transmission performance with 146 interfering channels versus wavelength (a) Q^2-factor for B2B and 50 km transmission; (b) Q^2-factor penalty; (c) B2B XY Q^2-factor difference.

observed, with a maximum of 1.2 dB at 1580 nm. A much larger, average penalty of ∼1.8 dB was observed in the S-band with a maximum value of 2.5 dB at 1470 nm. This penalty is due to the high NF of the DDRA in this region, resulting in a low output OSNR (Fig. 2), although higher nonlinearity in the S-band also plays a role in the overall performance degradation [46]. The Q^2-factor penalty in the E-band is similar in magnitude to the C- and L-bands, with an average of 0.7 dB, and a maximum of 1.2 dB at 1410 nm. The lower penalty in the E-band region is due to the low effective NF of the DDRA, clearly showing the benefit of distributed amplification for these channels.

The challenges of MBT using C-band components can be seen from the Q^2-factor difference between the two polarizations for the B2B setup as shown in Fig. 4(c). In the C- and L-band regimes, this imbalance was relatively small and largely uniform, with values < 0.5 dB over the entire bandwidth. A higher value of polarization imbalance can be seen for the shorter wavelength channels, rising from 0.7 dB at 1470 nm to a maximum of 1.6 dB at 1410 nm, and is one of the main factors degrading the Q^2-factor in the E-band [42].

IV. MODELLING OF THE HYBRID DDRA

This section describes the model used to estimate the MBT system performance. To that end, the impairments arising from the transceiver (TRX) (also referred to back-to-back (B2B) performance), optical amplifiers to compensate for the fibre loss, and fibre nonlinearity need to be taken into account. Assuming that all these three impairment factors can be modelled as statistically independent additive noise sources, the total received signal-to-noise ratio (SNR) for the i th WDM channel (SNR_i) after n spans is expressed as

$$\text{SNR}_i^{-1} \approx \text{SNR}_{\text{TRX}}^{-1} + \text{SNR}_{\text{ASE}}^{-1} + \text{SNR}_{\text{NLI}}^{-1}$$
$$= \left(\frac{P_i}{\kappa_i P_i + n P_{\text{ASE}_i} + \eta_n(f_i) P_i^3} \right)^{-1}, \quad (1)$$

where SNR_{TRX}, SNR_{ASE} and SNR_{NLI} is the SNR from the transceiver subsystem or back-to-back implementation penalty, the ASE from the optical amplifier used to compensate for the fibre loss and the accumulated NLI, respectively. Moreover, n

is the number of spans, i is the channel under consideration, P_i is its launch power, $\kappa_i = 1/\text{SNR}_{\text{TRX}_i}$, P_{ASE_i} is the ASE noise power, and $P_{\text{NLI}_i} = \eta_n(f_i) P_i^3$ is the NLI noise power after n spans.

For Raman-amplified links, the evolution of the channel/pump launch power is obtained from solutions to a set of nonlinear coupled equations [47], given by

$$\pm \frac{\partial P_i}{\partial z} = -\sum_k \frac{f_k}{f_i} g(\Delta f) P_k P_i + \sum_k g(\Delta f) P_k P_i - \alpha_i P_i, \quad (2)$$

where P_i, f_i is the power and frequency of the channel/pump of interest, and P_k, f_k are the power and frequency of the remaining WDM channels and pumps. Here, the pumps are considered as additional indices i, k in (2), $g_r(\Delta f)$ is the polarization averaged Raman gain spectrum, normalized by the effective core area A_{eff} for a frequency separation $\Delta f = |f_i - f_k|$, and α_i is the frequency-dependent attenuation coefficient. Note that the symbol $\pm$ represents the pump equation under consideration, i.e., $+$ and $-$ for forward (FW) and backward (BW) pump configuration, respectively.

The ASE noise power, P_{ASE_i}, from the Raman amplifier at the frequency of the ith channel is calculated as

$$P_{\text{ASE},i} = 2(G_i - 1) n_{sp} h f_i B_i, \quad (3)$$

where $n_{sp} \approx NF/2$ is the spontaneous emission factor, h is Planck's constant, and $G_i = P_{on}(L)/P_{off}(L)$ is the Raman amplifier on-off gain at the frequency of the ith channel, where $P_{on}(L)$ and $P_{off}(L)$ are the powers of channel i at the output of the Raman amplifier, in the presence and absence of pumps respectively. The NF values are an interpolation of the measured NF shown in Fig. 2. Note that, (3) can be used as an approximation to estimate the ASE noise generated by Raman amplification provided a characterisation of the amplifier NF is available. Otherwise, a full ASE modelling is required, such as for instance, the one presented in [48].

The nonlinear coefficient $\eta_n(f_i)$ is calculated for each one of the fibres. For the SMF, where the DiRA occurs, we use the

semi-analytical model in [32]:

$$\eta_n(f_i) \approx \sum_{j=1}^{n} \left[\frac{P_{i,j}}{P_i}\right]^2 \left[\eta_{\mathrm{SPM}_j}(f_i)n^\epsilon + \eta_{\mathrm{XPM}_j}(f_i)\right], \quad (4)$$

where $\eta_{\mathrm{SPM}_j}(f_i)$ is the contribution to the NLI coefficient due to SPM and $\eta_{\mathrm{XPM}_j}(f_i)$ is the contribution due to XPM from all the other WDM channels. $P_{i,j}$ is the power of channel i launched into the jth span, ϵ is the coherent factor [49, Eq. 22]. Closed-form approximations for $\eta_{\mathrm{SPM}}(f_i)$ and $\eta_{\mathrm{XPM}}(f_i)$ were derived in [32], [33], and are given respectively by

$$\eta_{\mathrm{SPM}}(f_i) = \frac{16}{27}\frac{\gamma^2}{B_i^2} \sum_{\substack{0 \le l_1+l_2 \le 1 \\ 0 \le l_1'+l_2' \le 1}} \Upsilon_i \Upsilon_i' \frac{\pi}{\phi_i(\alpha_{l,i}+\alpha_{l,i}')}$$

$$\times \left\{ 2(\kappa_{f,i}\kappa_{f,i}'+\kappa_{b,i}\kappa_{b,i}') \left[\mathrm{asinh}\left(\frac{3\phi_i B_i^2}{8\pi\alpha_{l,i}}\right)\right.\right.$$

$$+ \mathrm{asinh}\left(\frac{3\phi_i B_i^2}{8\pi\alpha_{l,i}'}\right)\right] + 4\ln\left(\sqrt{\frac{\phi_i L}{2\pi}}B_i\right)$$

$$\times \left[-(\kappa_{f,i}\kappa_{b,i}'+\kappa_{b,i}\kappa_{f,i}')\right.$$

$$\times \left(\mathrm{sign}\left(\frac{\alpha_{l,i}}{\phi_i}\right)e^{-|\alpha_{l,i}L|} + \mathrm{sign}\left(\frac{\alpha_{l,i}'}{\phi_i}\right)e^{-|\alpha_{l,i}'L|}\right)$$

$$+ (\kappa_{f,i}\kappa_{b,i}'-\kappa_{b,i}\kappa_{f,i}')$$

$$\left.\left.\times \left(\mathrm{sign}\left(-\phi_i\right)e^{-|\alpha_{l,i}L|}\mathrm{sign}\left(\phi_i\right)e^{-|\alpha_{l,i}'L|}\right)\right]\right\} \quad (5)$$

and

$$\eta_{\mathrm{XPM}}(f_i) = \frac{32}{27}\sum_{k=i,k\neq i}^{N_{ch}} \frac{\gamma^2}{B_k}\left(\frac{P_k}{P_i}\right)^2$$

$$\times \sum_{\substack{0 \le l_1+l_2 \le 1 \\ 0 \le l_1'+l_2' \le 1}} \Upsilon_k \Upsilon_k' \left(\frac{n+\frac{5}{6}\Phi_k}{\phi_{i,k}}\right.$$

$$\times \left\{ \frac{2(\kappa_{f,k}\kappa_{f,k}'+\kappa_{b,k}\kappa_{b,k}')}{\alpha_{l,k}+\alpha_{l,k}'}\left[\mathrm{atan}\left(\frac{\phi_{i,k}B_i}{2\alpha_{l,k}}\right)\right.\right.$$

$$\left.+ \mathrm{atan}\left(\frac{\phi_{i,k}B_i}{2\alpha_{l,k}'}\right)\right]$$

$$+ \pi\left[-\frac{\kappa_{f,k}\kappa_{b,k}'+\kappa_{b,k}\kappa_{f,k}'}{\alpha_{l,k}+\alpha_{l,k}'}\left(\mathrm{sign}\left(\frac{\alpha_{l,k}}{\phi_{i,k}}\right)e^{-|\alpha_{l,k}L|}\right.\right.$$

$$\left.+ \mathrm{sign}\left(\frac{\alpha_{l,k}'}{\phi_{i,k}}\right)e^{-|\alpha_{l,k}'L|}\right) + \frac{\kappa_{f,k}\kappa_{b,k}'-\kappa_{b,k}\kappa_{f,k}'}{\alpha_{l,k}+\alpha_{l,k}'}$$

$$\left.\left.\left.\times \left(\mathrm{sign}(-\phi_{i,k})e^{-|\alpha_{l,k}L|}+\mathrm{sign}(\phi_{i,k})e^{-|\alpha_{l,k}'L|}\right)\right]\right\}\right.$$

$$+ \frac{5}{6}\Phi_k\left[\frac{2\pi\tilde{n}(\kappa_{f,k}-\kappa_{b,k})(\kappa_{f,k}'-\kappa_{b,k}')}{|\tilde{\phi}_k|B_k^2\alpha_{l,k}\alpha_{l,k}'}\right.$$

$$\left.\left.\times \left((2\Delta f - B_k)\ln\left(\frac{2\Delta f - B_k}{2\Delta f + B_k}\right)+2B_k\right)\right]\right) \quad (6)$$

where

$$\phi_i = -4\pi^2\left(\beta_2 + 2\pi\beta_3 f_i\right),$$

$$\phi_{i,k} = -4\pi^2\left(f_k - f_i\right)\left[\beta_2 + \pi\beta_3\left(f_i + f_k\right)\right],$$

$$\tilde{\phi}_k = -4\pi^2[\beta_2 + \pi\beta_3(f_i + f_k)]L,$$

$$\Upsilon_i = T_i\left(\frac{-T_{f,i}}{T_i}\right)^{l_1}\left(\frac{T_{b,i}}{T_i}\right)^{l_2},$$

$$T_{f,i} = -\frac{P_f C_{f,i}(f_i - \hat{f})}{\alpha_{f,i}}, \quad T_i = 1 + T_{f,i} - T_{b,i}e^{-\alpha_{b,i}L},$$

$$\alpha_{l,i} = \alpha_i + l_1\alpha_{f,i} - l_2\alpha_{b,i},$$

$$T_{b,i} = -\frac{P_b C_{b,i}(f_i - \hat{f})}{\alpha_{b,i}}, \quad \kappa_{f,i} = e^{-(\alpha_i + l_1\alpha_{f,i})L},$$

$$\kappa_{b,i} = e^{-l_2\alpha_{b,i}L}.$$

The coefficient Υ_i' is respectively the same as in the above equations but with the indices l_1 and l_2 replaced by l_1' and l_2'. Similar notation is used for the variables $\alpha_{l,i}'$, $\kappa_{f,i}'$ and $\kappa_{b,i}'$. γ is the nonlinear parameter, β_2 is the group velocity dispersion (GVD) parameter, and β_3 is the linear slope of the GVD parameter. L is the span length, α_i, $\alpha_{f,i}$ and $\alpha_{b,i}$ are fibre attenuation coefficients, $\hat{f}$ is the average frequency of the FW and BW pumps, P_f and P_b are the total launch power of the WDM channels together with any FW pumps and BW pumps, respectively, and $C_{f,i}$ and $C_{b,i}$ is the slope of a linear regression of the normalised Raman gain spectrum. Φ_k represents the excess kurtosis of the given constellation, providing statistical characteristics of the signal, and reflecting how the constellation deviates from a Gaussian one.

Note that, the coefficients α_i, $C_{f,i}$, $C_{b,i}$, $\alpha_{f,i}$, and $\alpha_{b,i}$ are channel-dependent parameters and therefore matched using nonlinear least-squares fitting to correctly reproduce the solution of the Raman differential equations in the presence of Raman amplification, which is obtained by numerically solving (2). This fitting procedure also avoids divergence solutions of (5) and (6), such as the ones where $\alpha_{l,k}, \alpha_{l',k} \to 0$. This is because such solutions would yield unrealistic signal power profiles, increasing the error function and thus, would be automatically discarded by the fitting optimisation routine. For full details, see [32], [33].

For the IDFs, $\eta_n(f_i)$ is calculated using SSFM simulations. This is because validations of the model in [32], [33] together with the integral GN model are required over these short-length high-nonlinear fibres. Moreover, the short-length characteristics of these fibres make SSFM simulations feasible in reasonable computational time. Indeed, the most complex NLI estimation is the one in the distributed fibre stage made of 50 km SSMF, which is performed using (5) and (6). Finally, the total NLI is a summation of the NLI produced in the SSMF stage together with that produced in the IDF stages.
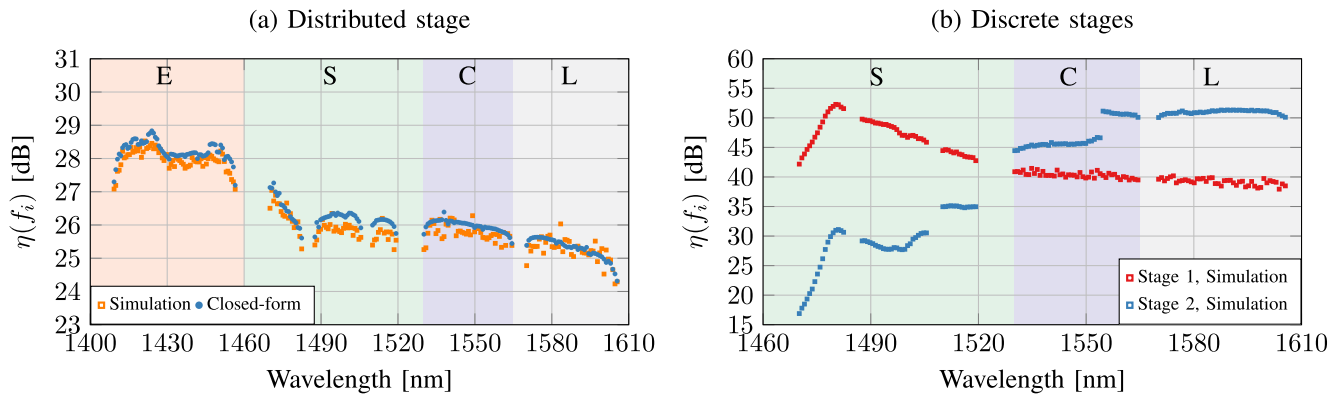
Fig. 5. Modelling of the nonlinear coefficient $\eta(f_i)$ for (a) distributed and (b) discrete Raman amplification stages.

V. MODELLING RESULTS OF THE COHERENT TRANSMISSION WITH THE HYBRID DDRA

In this section, we start by validating the predictions of (5) and (6) over the full E-, S-, C- and L- band transmission for a DiRA setup. After validation, we use the modelling strategy described in Section IV to estimate the total system performance. Further, we compare the results of this model with the experimental results described in Section II and III, showing reasonable agreement between the two. We follow this comparison with descriptions of further sets of simulations which consider additional scenarios, including a fully populated E-band, overcoming current limitations in the experimental infrastructure available. In addition, we consider the potential system performance improvements of an extra short-wavelength pump and the increase of certain short-wavelength pump powers.

A. Transmission System Setup

For the purposes of model validation, the same transmission system setup described in Section II and III is used, with the E-band fully populated with channels; this corresponds to 261 WDM channels spaced by 100 GHz, ranging from 1410 nm to 1605 nm, with each channel carrying −4 dBm launch power and modulated at a symbol rate of 30 GBaud. One distributed Raman amplification stage made of 50 km of SSMF and two discrete stages made of 7.5 km IDFs are considered. The pumps' wavelengths and powers for the distributed stage and for the discrete stage are described in Section II and illustrated in Fig. 1. Finally, each channel is modulated using 16-QAM constellations; this is achieved by setting the excess kurtosis $\Phi = -0.6800$ in (6).

For the distributed Raman amplification stage, where all the WDM channels are transmitted, the nonlinear coefficient and dispersion parameters are $\gamma = 1.3$ W^{-1}km^{-1}, $D = 17$ ps nm^{-1}km^{-1}, $S = 0.09$ ps nm^{-2}km^{-1}, respectively. For the discrete Raman amplification stages, where only the channels located in the S-, C- and L- bands are transmitted, these parameters are $\gamma = 3.53$ W^{-1}km^{-1}, $D = -44$ ps nm^{-1}km^{-1}, and $S = 0.003$ ps nm^{-2}km^{-1}, respectively. These values are obtained from datasheets of these transmission fibres. Moreover, for both distributed and discrete stages, the measured attenuation

and Raman gain profiles of these fibres are used [37]. The remaining parameters are the same as the ones described in Sections II and III.

B. Modelling Validation

The nonlinear coefficient $\eta(f_i)$ is shown in Fig. 5 for (a) the DiRA stage and (b) the DRA stages. For the DiRA stage, the nonlinear coefficient is calculated using the transmission system described in Section V-A and the analytical model described in Section IV by (5) and (6), while for the discrete stages, this coefficient is calculated with SSFM simulations only. This is because accuracy validations of the GN model for estimating the NLI in short-length highly-nonlinear fibres are further required. $\eta(f_i)$ is then calculated independently in each stage. To that end, the launch power at the end of each stage is used as input for the following stage.

For the distributed stage, the accuracy of the results of the modelling in Section IV are validated using the SSFM simulations. To ensure accurate simulation results in a reasonable time, adaptive step sizes with a local-error method was used, with goal local error $\delta_G = 10^{-10}$ [50]. Each channel had a random 2^{17} 16-QAM symbol sequence to ensure small η deviation between channels and reduce random simulation artifacts in the results. In terms of accuracy, Fig. 5(a) shows a maximum error of 0.74 dB computed between the closed form-expression in (5) and (6) and the SSFM simulations.

As shown in Fig. 5, for the DiRA stage, the higher NLI in the E-band is the result of the Raman amplification, which was designed to give gains in that band. A similar trend is observed for the discrete stages, wherein the first stage of the amplifier was designed to give preferential gain in the S-band, while the second stage was designed to give preferential gain in the C and L bands [27].

Fig. 6(a) shows the power evolution after each one of the fibre stages, obtained using (2) and the transmission setup described in Section V-A. Again, the launch power at the end of each stage is used as input for the following stage. Note that, though the distributed part of the experiment described in Section III was intended to give full power gain in the E-band, the modelling shows that the distributed pump setup is insufficient to fully
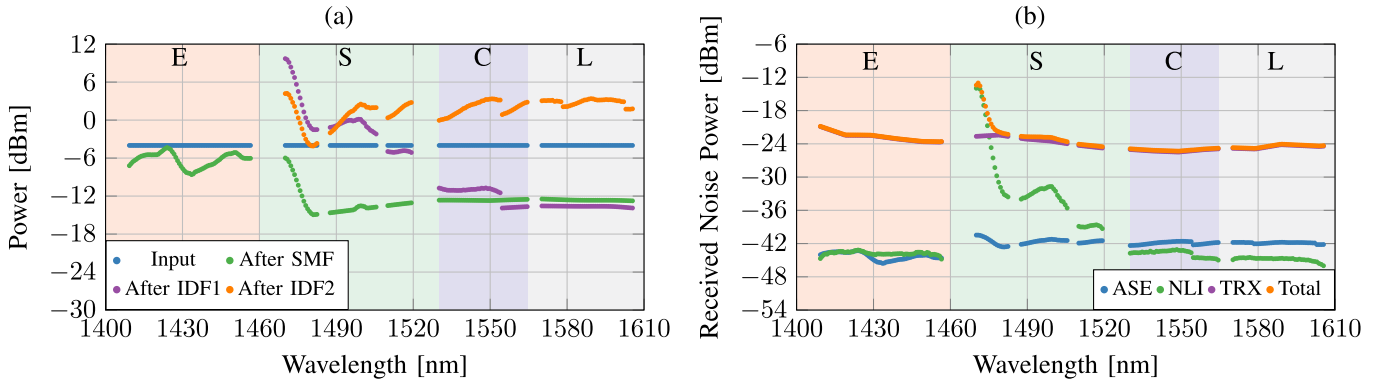
Fig. 6. Modelling of (a) launch power profile evolution after each Raman amplified stage and (b) received noise power profile contributions from ASE, NLI, TRX and the total after DDRA.
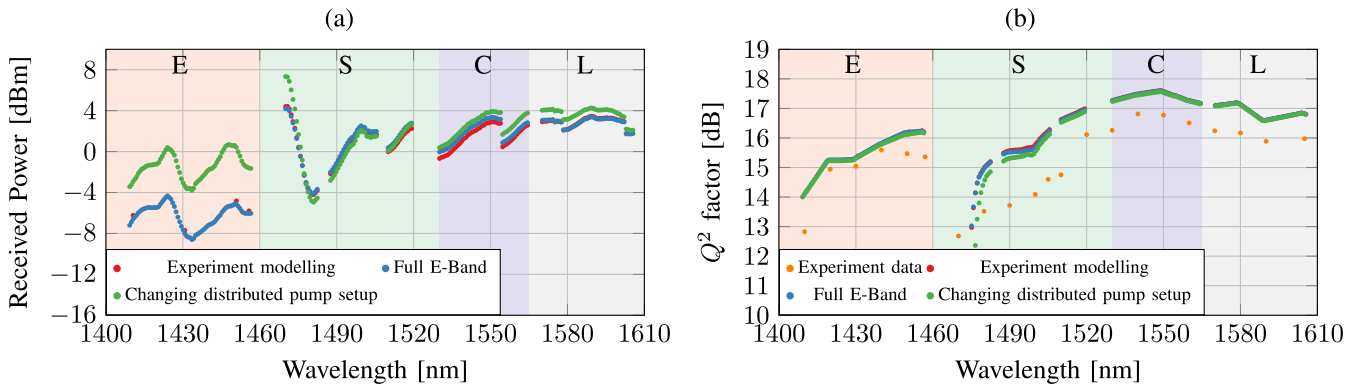

Fig. 7. Received (a) per-channel power after DDRA and (b) Q^2-factor for the scenarios described in Section V-C.

recover the transmitted signal power spectrum in that band, requiring a modification on the pump setup for the distributed stage in order to achieve that goal; this is explored in Section V-C.

Fig. 6(b) shows the received noise power levels for each one of the noise contributions. The total NLI noise is calculated by summing the NLI generated in each one of the stages using (5) and (6). The total ASE noise is calculated using (3) where the on-off amplifier gains G_i is computed using (2) in the presence and absence of pumps. The NF used in this equation is obtained from an interpolation of the measured data shown in Fig. 2, while the TRX noise is an interpolation of the measured data shown in Fig. 4(a). Finally, the total received noise is the summation of all the different noise contributions (ASE, NLI and TRX). Moreover, from Fig. 6(b) it is noted that the transceiver noise limits the total noise power for the E, C and L bands. However, in the shortest S-band channels, the NLI noise also contributes significantly to the total noise power.

C. Transmission Experiment Modelling and Improvements

Having established the model validation for a full E-, S-, C- and L- band transmission in Section V-B for the MBT DDRA-based system described in Section V-A, we now proceed to the direct modelling of our experiment. To that end, we

consider only 4-channels in the E-band also modulated using 16-QAM constellations, as described in Section III. For this scenario, Fig. 7 shows (a) the received power profile and (b) the Q^2-factor calculated after all the amplification stages, both indicated as red markers. The term "received power" refers to the power at the span output after the hybrid DDRA and before the OBPF. The Q^2-factor obtained from the experimental data, measured in Section III and shown in Fig. 4, is also shown in this figure as orange markers. In terms of accuracy, when comparing the modelling with the experimental data, a typical Q^2-factor error of ∼1 dB was found, with a maximum error of 1.8 dB in the S-band. The authors believe that this discrepancy is due to a combination of experimental factors which are not fully considered in the modelling, including component losses, polarisation imbalances, scattering effects and additional nonlinearity-induced products generated by the pumps falling within the signal band, which are not captured by the model and simulations.

As mentioned in Section V-B, the distributed Raman pump setup is not capable of fully amplifying the E-band. To that end, we consider another simulation scenario, where we augment the distributed pump setup to achieve full amplification in the E-band, by adding an additional 500 mW pump at 1305 nm and allowing increase of the 1325 and 1345 nm pumps by

100 mW each. This results in a modified distributed pump setup, corresponding to a total of 4 pumps located at 1305, 1325, 1345 and 1365 nm, with powers of 500, 539, 253 and 318 mW, respectively. Modelling predictions corresponding to this modified scenario are illustrated as green marks in Fig. 7, showing that this straightforward change enables full E-band amplification (total power recovery) in practice. Note that, in Fig. 7, we also show the results for the full E-band transmissions described in Section V-A and V-B as blue markers.

Additionally, from Fig. 7(a) it is interesting to note that when the E-band is fully loaded with channels (blue markers), higher power is transferred from the E- to the S- and C- bands, increasing the power levels in these bands when compared to the experiment modelling (red markers) - this is a direct effect of ISRS. However, the increased level of ISRS has negligible impact on the C-band Q^2-factor, as shown in Fig. 7(b); this is because the performance in this band is limited by the TRX noise, i.e, the B2B performance [31]. On the other hand, the same analysis shows a slight decrease in S-band performance which is explained by noting that the performance of the shortest S-band channels starts to be dominated by the NLI noise (see Fig. 6(b)), which increases its power as a result of the ISRS effect.

VI. CONCLUSION

In this work, we have investigated the performance of multi-band transmission with a hybrid distributed-discrete Raman amplifier over the low loss, E-, S-, C- and L-band of the optical window. Experimental investigation showed successful transmission of 200 Gbit/s PM-16-QAM signals over 50 km of SSMF, well above the HD-FEC threshold of 8.5 dB. The transmission results also indicated the effects of polarization imbalance of the shorter wavelength E-band channels in multi-band transmission systems, when using transceivers based on components optimised for the C-band. Analytical modelling was performed for the developed amplifier and compared to SSFM simulations where a maximum error of 0.74 dB was observed for the E-band channels amplified by the distributed amplification stage. In the dual-stage discrete amplifier stage, amplifying the S-, C-, and L-bands, the modelling was performed using SSFM simulations, for which a maximum per-channel Q^2-factor deviation of 1.8 dB was observed versus the experimental results.

The modelling simulations also showed that in the presence of a fully loaded E-band, received power in that band cannot be fully recovered with the current experimental setup. Hence, it was shown that modification of the distributed stage with an additional 500 mW pump at 1305 nm, together with an increase of 100 mW in the pump powers at 1325 nm and 1345 nm could achieve the desired E-band signal power levels, necessary to support multi-span links.

REFERENCES

[1] P. J. Winzer, D. T. Neilson, and A. R. Chraplyvy, "Fiber-optic transmission and networking: The previous 20 and the next 20 years," *Opt. Exp.*, vol. 26, no. 18, pp. 24190–24239, Sep. 2018.

[2] H. Sun et al., "800G DSP ASIC design using probabilistic shaping and digital sub-carrier multiplexing," *J. Lightw. Technol.*, vol. 38, no. 17, pp. 4744–4756, Sep. 2020.

[3] M. Secondini and E. Forestieri, "Scope and limitations of the nonlinear Shannon limit," *J. Lightw. Technol.*, vol. 35, no. 4, pp. 893–902, Feb. 2017.

[4] D. J. Richardson, J. M. Fini, and L. E. Nelson, "Space-division multiplexing in optical fibres," *Nature Photon.*, vol. 7, no. 5, pp. 354–362, 2013.

[5] G. Rademacher et al., "10.66 peta-bit/s transmission over a 38-core-three-mode fiber," in *Proc. Opt. Fiber Commun. Conf. Exhib.*, 2020, pp. 1–3.

[6] R. S. Luis, B. J. Puttnam, G. Rademacher, Y. Awaji, and H. Furukawa, "372 Tb/s unrepeatered 213 km transmission over a 125 µm cladding diameter, 4-core MCF," in *Proc. Opt. Fiber Commun. Conf. Exhib.*, 2022, pp. 1–3.

[7] B. J. Puttnam, R. S. Luís, G. Rademacher, Y. Awaji, and H. Furukawa, "High-throughput and long-distance transmission with nm s-, c- and l-band signal in a 125 µm 4-core fiber," *J. Lightw. Technol.*, vol. 40, no. 6, pp. 1633–1639, Mar. 2022.

[8] A. Ferrari et al., "Assessment on the achievable throughput of multi-band ITU-T G.652.D fiber transmission systems," *J. Lightw. Technol.*, vol. 38, no. 16, pp. 4279–4291, Aug. 2020.

[9] T. Hoshida et al., "Ultrawideband systems and networks: Beyond C+L-band," *Proc. IEEE*, vol. 110, no. 11, pp. 1725–1741, Nov. 2022.

[10] J. Renaudier et al., "Devices and fibers for ultrawideband optical communications," *Proc. IEEE*, vol. 110, no. 11, pp. 1742–1759, Nov. 2022.

[11] R. Emmerich et al., "Enabling S-C-L-band systems with standard C-band modulator and coherent receiver using coherent system identification and nonlinear predistortion," *J. Lightw. Technol.*, vol. 40, no. 5, pp. 1360–1368, Mar. 2022.

[12] N. K. Fontaine, M. Mazur, R. Ryf, H. Chen, L. Dallachiesa, and D. T. Neilson, "36-THz bandwidthwavelength selective switch," in *Proc. Eur. Conf. Opt. Commun.*, 2021, pp. 1–4.

[13] R. Kraemer et al., "Multi-band photonic integrated wavelength selective switch," *J. Lightw. Technol.*, vol. 39, no. 19, pp. 6023–6032, Oct. 2021.

[14] L. Rapp and M. Eiselt, "Optical amplifiers for multi–band optical transmission systems," *J. Lightw. Technol.*, vol. 40, no. 6, pp. 1579–1589, Mar. 2022.

[15] F. Pittala et al., "72.64 TB/s DWDM transmission over 100 KM G.654D fiber using super C-band erbium-doped fibre amplification," in *Proc. Opt. Fiber Commun. Conf.*, 2022, Paper W3C–4.

[16] L. Wang et al., "Low cost solution for super lLband fiber amplifier based on single-mode and multi-mode hybrid pumping scheme," in *Proc. Opt. Fiber Commun. Conf.*, 2022, Paper W3J–4.

[17] J. Mirza, S. A. Ghafoor, N. Habib, F. Kanwal, and K. K. Qureshi, "Performance evaluation of praseodymium doped fiber amplifiers," *Opt. Rev.*, vol. 28, pp. 611–618, 2021.

[18] J. Dawson et al., "E-band Nd^{3+} amplifier based on wavelength selection in an all-solid micro-structured fiber," *Opt. Exp.*, vol. 25, pp. 6524–6538, 2017.

[19] A. Donodin et al., "Bismuth doped fibre amplifier operating in E- and S- optical bands," *Opt. Mater. Exp.*, vol. 11, no. 1, pp. 127–135, Jan. 2021.

[20] J. Renaudier et al., "First 100-nm continuous-band WDM transmission system with 115 Tb/s transport over 100 km using novel ultra-wideband semiconductor optical amplifiers," in *Proc. Eur. Conf. Opt. Commun.*, 2017, pp. 1–3.

[21] A. Ghazisaeidi et al., "99.35 Tb/s ultra-wideband unrepeated transmission over 257 km using semiconductor optical amplifiers and distributed Raman amplification," *J. Lightw. Technol.*, vol. 40, no. 21, pp. 7014–7019, Nov. 2022.

[22] W. S. Pelouch, "Raman amplification: An enabling technology for long-haul coherent transmission systems," *J. Lightw. Technol.*, vol. 34, no. 1, pp. 6–19, Jan. 2016.

[23] S. Namiki and Y. Emori, "Ultrabroad-band Raman amplifiers pumped and gain-equalized by wavelength-division-multiplexed high-power laser diodes," *IEEE J. Sel. Topics Quantum Electron.*, vol. 7, no. 1, pp. 3–16, Jan./Feb. 2001.

[24] P. Hazarika, M. Tan, and W. Forysiak, "Recent advances in wideband Raman amplifiers," *Next-Gener. Opt. Commun.: Compon., Sub-Syst., Syst. XII*, vol. 12429, 2023, pp. 143–145.

[25] L. Krzczanowicz et al., "Low transmission penalty dual-stage broadband discrete Raman amplifier," *Opt. Exp.*, vol. 26, no. 6, pp. 7091–7097, Mar. 2018.

[26] M. A. Iqbal, L. Krzczanowicz, I. Phillips, P. Harper, and W. Forysiak, "150 nm SCL-Band transmission through 70 km SMF using ultra-wideband dual-stage discrete raman amplifier," in *Proc. Opt. Fiber Commun. Conf.*, 2020, Paper W3E.

[27] P. Hazarika et al., "Ultra-wideband discrete Raman amplifier optimization for single-span S-C-L-band coherent transmission systems," *Opt. Lett.*, vol. 47, no. 24, pp. 6472–6475, Dec. 2022.

[28] P. Hazarika et al., "210 nm E, S, C and L band multistage discrete Raman amplifier," in *Proc. Opt. Fiber Commun. Conf.*, 2022, Paper Tu3E.2.

[29] P. Hazarika et al., "E-coherent transmission with a multistage discrete Raman amplifier," *Opt. Exp.*, vol. 30, no. 24, pp. 43118–43126, Nov. 2022.

[30] R. Matzner, D. Semrau, R. Luo, G. Zervas, and P. Bayvel, "Making intelligent topology design choices: Understanding structural and physical property performance implications in optical networks," *J. Opt. Commun. Netw.*, vol. 13, no. 8, pp. D53–D67, Aug. 2021.

[31] H. Buglia, E. Sillekens, A. Vasylchenkova, P. Bayvel, and L. Galdino, "On the impact of launch power optimization and transceiver noise on the performance of ultra-wideband transmission systems [invited]," *J. Opt. Commun. Netw.*, vol. 14, no. 5, pp. B11–B21, May 2022.

[32] H. Buglia, M. Jarmolovičius, L. Galdino, R. I. Killey, and P. Bayvel, "A closed-form expression for the Gaussian noise model in the presence of Raman amplification," *J. Lightw. Technol.*, early access, Sep. 13, 2023, doi: 10.1109/JLT.2023.3315127.

[33] H. Buglia, M. Jarmolovicius, L. Galdino, R. I. Killey, and P. Bayvel, "A modulation-format dependent closed-form expression for the Gaussian noise model in the presence of Raman amplification," in *Proc. Eur. Conf. Opt. Commun.*, 2023, pp. 1–3.

[34] U. C. De Moura et al., "Multi–band programmable gain Raman amplifier," *J. Lightw. Technol.*, vol. 39, no. 2, pp. 429–438, Jan. 2021.

[35] C. Lasagni, P. Serena, A. Bononi, and J.-C. Antona, "A generalized Raman scattering model for real-time SNR estimation of multi-band systems," *J. Lightw. Technol.*, vol. 41, no. 11, pp. 3407–3416, Jun. 2023.

[36] P. Hazarika, A. Donodin, M. Tan, I. Phillips, P. Harper, and W. Forysiak, "30-Gbaud PM-16-QAM transmission over E-, S-, C- and L-band with hybrid Raman amplifier," in *Proc. Opt. Fiber Commun. Conf.*, 2023, pp. 1–3.

[37] P. Hazarika et al., "Performance evaluation of discrete Raman amplifiers in coherent transmission systems," *Opt. Exp.*, vol. 30, no. 24, pp. 43053–43061, Nov. 2022.

[38] M. A. Iqbal, P. Harper, and W. Forysiak, "Improved design of ultra-wideband discrete raman amplifier with low noise and high gain," in *Proc. Adv. Photon.* 2018, Paper NpTh1H–2.

[39] S. Liang et al., "High gain, low noise, spectral-gain-controlled, broadband lumped fiber Raman amplifier," *J. Lightw. Technol.*, vol. 39, no. 5, pp. 1458–1463, Mar. 2021.

[40] M. A. Iqbal et al., "Impact of pump-signal overlap in SCL band discrete Raman amplifiers," *Opt. Exp.*, vol. 28, no. 12, pp. 18440–18448, Jun. 2020.

[41] ITU-T, "G.698.2 : Amplified multichannel dense wavelength division multiplexing applications with single channel optical interfaces," Int. Telecommun. Union, G.698.2(11/18), pp. 1–48, Nov. 2018. [Online]. Available: itu.int/rec/T-REC-G.698.2-201811-I

[42] R. Emmerich et al., "Enabling S-C-L-Band systems with standard C-band modulator and coherent receiver using coherent system identification and nonlinear predistortion," *J. Lightw. Technol.*, vol. 40, no. 5, pp. 1360–1368, Mar. 2022.

[43] A. Donodin et al., "30-GBaud DP 16-QAM transmission in the E-band enabled by bismuth-doped fiber amplifiers," *Opt. Lett.*, vol. 47, no. 19, pp. 5152–5155, Oct. 2022.

[44] A. D. Ellis, M. E. McCarthy, M. A. Z. Al Khateeb, M. Sorokina, and N. J. Doran, "Performance limits in optical communications due to fiber nonlinearity," *Adv. Opt. Photon.*, vol. 9, no. 3, pp. 429–503, Sep. 2017.

[45] R. Emmerich, C. Schmidt-Langhorst, C. Schubert, and R. Freund, "Characterization of C-band coherent receiver front-ends for transmission systems beyond S-C-L-band," *IEEE Photon. Technol. Lett.*, vol. 35, no. 22, pp. 1231–1234, Nov. 2023.

[46] M. A. Iqbal, M. A. Z. Al-Khateeb, L. Krzczanowicz, I. D. Phillips, P. Harper, and W. Forysiak, "Linear and nonlinear noise characterisation of dual stage broadband discrete raman amplifiers," *J. Lightw. Technol.*, vol. 37, no. 14, pp. 3679–3688, Jul. 2019.

[47] V. E. Perlin and H. G. Winful, "Optimizing the noise performance of broad-band WDM systems with distributed raman amplification," *IEEE Photon. Technol. Lett.*, vol. 14, no. 8, pp. 1199–1201, Aug. 2002.

[48] D. Dahan and G. Eisenstein, "The properties of amplified spontaneous emission noise in saturated fiber Raman amplifiers operating with CW signals," *Opt. Commun.*, vol. 236, no. 4, pp. 279–288, 2004.

[49] P. Poggiolini, "The GN model of non-linear propagation in uncompensated coherent optical systems," *J. Lightw. Technol.*, vol. 30, no. 24, pp. 3857–3879, Dec. 2012.

[50] O. V. Sinkin, R. Holzlohner, J. Zweck, and C. R. Menyuk, "Optimization of the split-step Fourier method in modeling optical-fiber communications systems," *J. Lightw. Technol.*, vol. 21, no. 1, pp. 61–68, Jan. 2003.